Heat transfer characteristics and compatibility of molten salt/ceramic porous composite phase change material

Shuai Zhang[a], *Ziyuan Li*[b], *Yuanpeng Yao*[a], *Limei Tian*[b], *Yuying Yan*[a,*]

[a] Faculty of Engineering, University of Nottingham, University Park, Nottingham, UK

[b] Key Laboratory of Bionic Engineering (Ministry of Education), Jilin University, Changchun, China

* Corresponding author, E-mail: Yuying.Yan@nottingham.ac.uk

ABSTRACT

Molten salts are popular energy storage materials for medium- and high-temperature thermal energy storage. However, current methods for heat transfer enhancement do not apply due to the high corrosivity of molten salts and extreme high-temperature environment. Herein, porous silicon carbide (SiC) ceramic and solar salt are formed into a composite phase change material (PCM). The ceramic skeleton is fabricated to an open-cell structure with high porosity and a large pore configuration. The SiC ceramic is wetted by the solar salt, so that the impregnation of salt into ceramic achieves a high loading at atmospheric pressure. The result of visual inspection shows that the temperature distribution in the composite PCM is more uniform compared with pure solar salt. The maximum temperature difference is reduced from 148℃ to 130℃ and the overall phase change rate is increased by up to 42.9%. The SiC ceramics show excellent corrosion resistance during the cycles of thermal charging and discharging as compared to copper and aluminium which are the widely used thermal promoters for low-temperature PCMs. The results obtained from reactive molecular dynamics (MD) simulation are consistent with the corrosion behaviours of SiC ceramic in solar salt from the aspects of physical dissolution, chemical reaction, and thermal stress failure. The composite PCM has

advantages of simple preparation, low cost, and easy maintenance, therefore it has a great potential for large-scale applications.

Keywords: high-temperature; ceramic; molten salt; porous; heat transfer; compatibility

1. Introduction

The thermal energy storage (TES) technique solves the mismatch between energy supply and demand by storing surplus thermal energy in phase change materials (PCMs) and releasing it when needed [1, 2]. According to the melting point of PCMs, TES is classified as low-temperature (melting point < 100℃), medium-temperature (melting point 100℃ ~ 300℃) and high-temperature (melting point > 300℃) ones [3]. Molten salts have been widely used as medium- and high-temperature energy storage materials due to their appropriate melting point, large energy storage density, low cost, excellent thermal stability, low vapour pressure, etc [4-6]. They have considerable application values in concentrated solar power [7], industrial waste heat recovery [8] and peak shaving of power grid [9]. However, pure salts commonly suffer from low thermal conductivity, for example, the thermal conductivity of KNO_3 is only around 0.5 W/m K [10], which limits the energy storage efficiency.

For low-temperature PCMs, there are many heat transfer enhancement methods such as adding fins [11, 12], metal foams [13-15], etc. However, for the medium- and high-temperature PCMs, these methods may be not applicable. It is not only because some thermal promoters will soften even decompose due to the extreme high-temperature environment; but also because they may be incompatible with molten salt due to the high corrosivity of salts. Moreover, the thermal promoter must be low-cost so the TES technique is economically feasible.

Ceramics have inherently high thermal conductivity, superior corrosion resistance and low cost [16-19]. Some researchers have used ceramic and molten salt to prepare shape-stabilised phase change materials (ss-PCMs) [20, 21]. The pore size of ss-PCMs is in the magnitude of micron and nanometer [22, 23]. Ss-PCMs are commonly used to prevent leakage by restricting the flow of liquid salt through capillary force and surface tension. However, the porosity of ss-PCMs is only about 0.6 or less [22, 24], which means the energy storage density is low. Moreover, the micro- and nano-pores exert strong restrictions on the fluid flow and the natural

convection heat transfer is almost eliminated. Additionally, once the skeleton and PCM are integrated together, it is very difficult to separate them. If the skeleton or salt fails, the whole ss-PCM needs to be replaced, rather than only maintaining the single skeleton or salt, which increases the maintenance cost. It is desirable to design a new ceramic-based PCM with a large porosity and open cells to address the energy density, heat transfer and maintenance issues.

Phase change heat transfer is of fundamental importance for determining thermal-fluidic behaviours of PCMs and evaluating TES system performance. Some researchers have carried out experimental and numerical studies on the phase change heat transfer of porous composite PCMs [25-28]. The main mechanisms in phase change heat transfer are heat conduction and natural convection. Through making full use of natural convection, the better comprehensive performance of the TES unit can be achieved with a high-porosity skeleton [29]. However, current studies mainly focus on low-temperature PCMs. Paraffin (melting point: 26℃-68℃ [30, 31]) and metal foams are the most used PCM and porous support respectively in the current researches [2]. Heat transfer characteristics of molten salt with porous ceramic skeleton are rarely reported, especially the visualised investigations. Additionally, corrosion is a key issue of molten salt-based PCM [32]. It is essential to test the compatibility between the ceramic skeleton and molten salt to ensure the durability of the thermal promoter.

In this paper, a novel ceramic/solar salt (60wt% $NaNO_3$ + 40wt% KNO_3) porous composite phase change material was prepared. The composite PCMs are open-cell and the pore size is 10 PPI, 15 PPI and 20 PPI. This pore configuration allows the fluid flow and benefits the natural convection. The porosity is high, up to 0.85, which guarantees the energy storage density. Moreover, the porous skeleton can be easily integrated with and extracted from solar salt, which enables maintaining the single salt and skeleton. Visualised experiments were conducted to investigate the phase change heat transfer characteristics including temperature evolution, melting fraction, solid-liquid phase interface and temperature field. Corrosion

behaviours of ceramic in the presence of solar salt were analysed using various characterising techniques, namely scanning electron microscope (SEM), energy-dispersive spectroscopy (EDS), X-ray diffraction (XRD) and Raman. Additionally, in order to provide microscopic insights into corrosion behaviours of ceramic, a reactive molecular dynamics (MD) simulation was performed. This study aims to provide a simple-preparation, low-cost and easy-maintenance composite PCM for potential large-scale applications.

2. Experiments

2.1 Material preparation

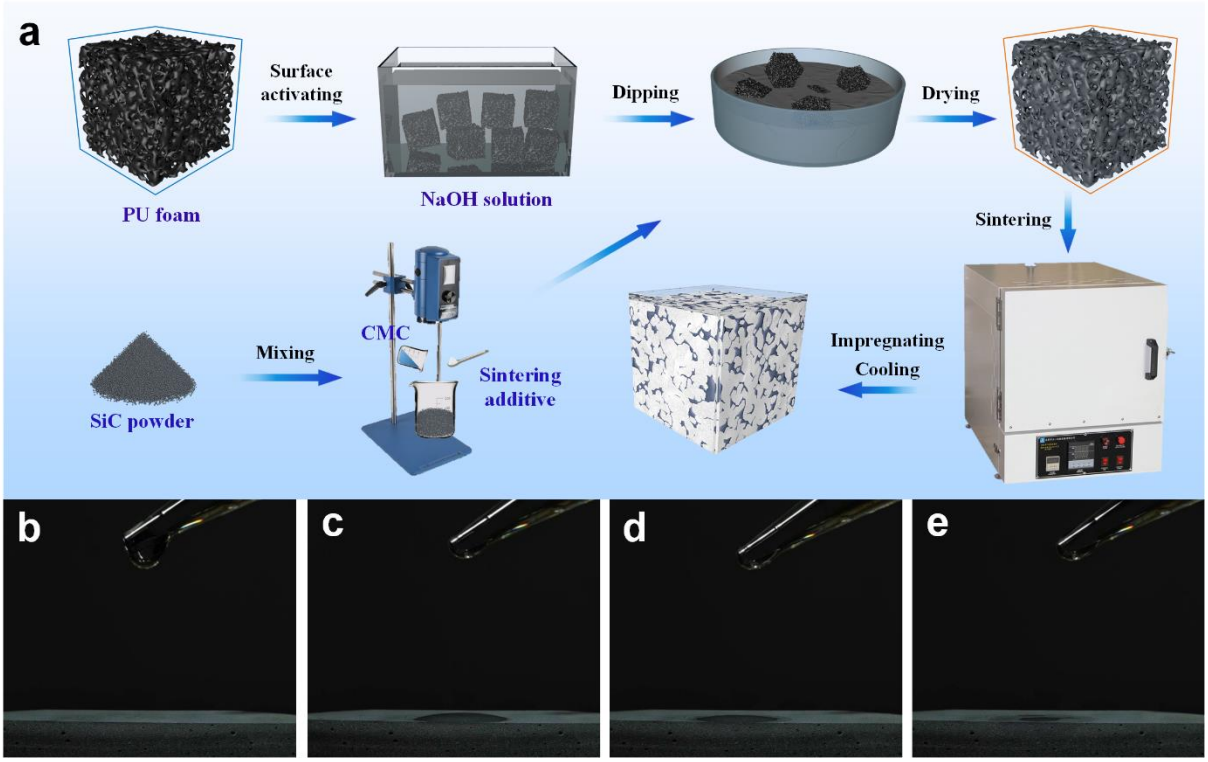

Figure 1. (a) Schematic of the preparation process of ceramic/molten salt porous composite phase change material. (b)-(e): Wetting behaviour of the molten solar salt drop to the ceramic substrate. Left to right figure corresponds to t = 0 ms, 300 ms, 600 ms and 1100 ms respectively.

The preparation process of ceramic/molten salt porous composite phase change material is shown in **Figure 1**(a). Polyurethane (PU) foams with the pore size of 10 pores per inch (PPI), 15 PPI and 20 PPI were used as carriers and supplied by Yueyang Sponge Co., Ltd. Industrial SiC ceramic powder (particle size:10 μm - 13 μm) was used as the base material of the ceramic

skeleton and purchased from Xianfeng Material Co., Ltd. Kaolin, alumina, yttrium oxide and polyvinyl alcohol were supplied by Yousuo Chemical Co., Ltd. Kaolin, alumina and yttrium oxide act as the binder while polyvinyl alcohol was employed to improve the adhesion of the ceramic slurry to PU foams. N-octanol was purchased from Kermel Chemical Co., Ltd. $NaNO_3$ and KNO_3 (purity $\geqslant$ 99.0%) were supplied by China National Pharmaceutical Co., Ltd. The nitrate salts were utilised to prepare solar salt (60wt% $NaNO_3$ + 40wt% KNO_3) which is a widely used PCM in medium-temperature thermal energy storage.

First, the PU foam (dimension: 50 mm × 50 mm × 50 mm; mass: 3.75g) was submerged in NaOH solution (concentration: 10wt%) for 12 h to activate the surface [33]. Then, it was dipped in the SiC ceramic slurry. The main components of the slurry are SiC powder, kaolin, alumina and yttrium oxide and the mass ratio is 86: 7: 4: 3. The mass fraction of these solid powders is 77.9%. Next, carboxymethylcellulose sodium (CMC) was added to increase the viscosity. Sodium polyacrylate and N-octanol were added as the dispersant and defoamer respectively. Silica sol and polyvinyl alcohol were utilised to improve the adhesion of the ceramic slurry to PU foams. The mass fractions of CMC, sodium polyacrylate, N-octanol, silica sol and polyvinyl alcohol are 17.8%, 0.2%, 0.1%, 3.7% and 0.3% respectively.

The ceramic slurry was first let stand for 24 hours. Subsequently, PU foams were dipped in the slurry and then squeezed using a roller machine to remove the excess slurry. Next, they were dried at 80 ℃ for 6 hours; then sintered in a furnace at 1400 ℃ for 2 hours. Both processes of the drying and the sintering are in the air atmosphere. The sintered ceramic matrix was impregnated into liquid solar salt, followed by cooling to obtain the final composite phase change material. Thermo-physical properties of solar salt including melting point, density, heat capacity and thermal conductivity can be found in Table S1 in the **Supporting Information**. The morphology of the final composite PCM is shown in Figure S2.

The wettability of the ceramic was tested by dropping the molten solar salt drop on the ceramic substrate. The bulk ceramic was sintered and was cut into a 5 cm × 5 cm × 2 cm piece (mass: 116.4g). Then it was placed on a copper plate heater. The temperature of the cooper heater was kept at 300 ℃ which was higher than the liquidus temperature of solar salt (246 ℃). This setup ensured that the solar salt on the ceramic substrate was liquid. The solar salt in a beaker was heated to melt. Then a straw was used to suck up the liquid salt. Next, the liquid salt was dropped on the ceramic substrate. As Figures 1(b)-(e) show, the salt drop infiltrates into the ceramic substrate easily, indicating the ceramic has excellent wettability to solar salt. This is very important for integrating PCM with the skeleton. The vacuum impregnation is usually employed to integrate low-temperature PCMs with the porous skeleton to improve the loading [2]. However, for molten salts, it is difficult to obtain the vacuum along with the high-temperature condition; and the equipment cost will be increased greatly. The excellent wettability of ceramic enables the atmospheric impregnation to achieve a high loading so that the impregnation process is cost-effective.

2.2 Thermal performance test

The phase change heat transfer characteristics were investigated using the experimental setup in **Figure 2**(a). The setup consists of computer, aluminium heater, K-type thermocouples (WRNK-191, Jiayi Electric Co., Ltd), temperature controller (AI-516P, Yudian Technology Co., Ltd), data collection system (KSA12A0R, Keshun Instrument Co., Ltd), infrared camera (HM-TPH16-6VF/W, Hikvision Technology Co., Ltd) and test section.

Three composite PCMs were used, which were prepared by infiltrating liquid solar salt into the ceramic matrix with the porosity of 0.85 and the pore size of 10 PPI, 15 PPI and 20 PPI. Atmospheric impregnation was utilized due to the excellent wettability of the ceramic to solar salt as discussed above and the impregnation ratio was measured to be over 95%. The dimension of composite PCMs was about 50 mm × 50 mm × 50 mm. The composite PCM was encaged

in a quartz cavity with the wall thickness of 2 mm, as shown in **Figure S2**. A gap of about 5 mm between the top surface of the composite and the top edges of the cavity was left to allow the expansion of molten salt. The left side of the quartz cavity was attached to an aluminium plate heater. The heater was kept 300 ℃ during the experiment. The accuracy of the temperature controller of the aluminium electrical heater is ±0.25%.

Three small round holes were drilled in the centre of the PCM, which were 25 mm in height and 5 mm (point P1), 25mm (point P2) and 45 mm (point P3) away from the left wall of the quartz cavity. Three K-type thermocouples were inserted into the holes to measure the temperature at points P1, P2 and P3. The thermocouples were calibrated against a standard thermometer with an accuracy of ±0.3%. Temperature data were collected every 1 minute. The schematic of thermocouples distribution is shown in **Figure S3**.

The quartz cavity was covered by thermal insulation materials to reduce the heat loss to the surroundings. An infrared camera was used to capture the temperature field of the front surface of the quartz cavity. The detailed parameters and calibration of the infrared camera are provided in the Supporting Information. A conventional camera was utilised to observe the solid-liquid interface. The front insulation material was removed every 10 minutes to take the picture of the melting process. The uncertainties of all parameters are summarised in **Table S3**. The phase change heat transfer experiment of the pure solar salt was also conducted to make a comparison.

2.3 Corrosion test

The ceramic block was sintered and used to investigate the corrosion behaviours. The sintered ceramic block was cut into pieces with the size of 10 mm × 10 mm × 2 mm, followed by polishing and drying. Then ceramic pieces were placed into alumina crucibles and buried by the solar salt. The crucibles were transferred to the furnace and heated from 150 ℃ to 300 ℃ with a heating rate of 10 ℃/min. Then the temperature was maintained at 300 ℃ for 30 min to

melt the solar salt completely. Subsequently, samples were cooled to 150 ℃ with a rate was 4 ℃/min, followed by cooling at 150 ℃ for 60 min.

There are four groups in the experiment: the first is the reference group with 0 heating/cooling cycle; the second, third and fourth group underwent 50, 100 and 200 cycles respectively. When the experiments were finished, samples were first washed using the flowing water to remove the salt on the surface. Then they were ultrasonically washed in the distilled water for 5 min to further remove the salt. Finally, they were dried at 40 ℃ for 3 h. Here, SEM, EDS (VEGA3, Tescan Instrument Co., Ltd), XRD (MAXima XRD-7000, Shimadzu Technology Co., Ltd) and Raman spectrometer (DXR SmartRaman, Thermo Fisher Scientific Inc.) were used to characterise ceramic pieces. To compare the corrosion behaviours, Cu and Al - the widely used metal heat promoter - were tested. The test of each metal also consists of four groups: reference group (0 cycle), 50 cycles group, 100 cycles group and 200 cycles group. The test condition of the metal is the same as that of ceramic.

3. Theoretical modelling

3.1 ReaxFF method

The ReaxFF reactive molecular dynamics (MD) was used to provide microscopic insights into corrosion behaviours of SiC ceramic. The ReaxFF method bridges the gap between computational quantum chemistry and traditional MD [34]. It allows the breaking and forming of bonds and is specifically designed to describe chemical reactions such as combustion [35], catalysis [36], corrosion [37], pyrolysis [38], etc. The ReaxFF method is an empirical force field the parameters of which are usually derived by fitting against a training set consisting of quantum mechanics (QM) and experimental data. It can obtain good accuracy for reaction energies and reaction barriers. Moreover, the computational expense is several orders of magnitude lower than the QM-based simulations, which makes the ReaxFF method an ideally suited tool for simulating large-scale and complex reacting systems [39].

The ReaxFF energy term is given by [40]:

$$E_{\text{total}} = E_{\text{bond}} + E_{\text{under}} + E_{\text{over}} + E_{\text{val}} + E_{\text{tors}} + E_{\text{lp}} + E_{\text{H-bond}} + E_{\text{vdW}} + E_{\text{Coulomb}} \quad (1)$$

where E_{bond} is the bond energy; E_{under} and E_{over} are the undercoordination penalty energy and overcoordination penalty energy respectively; E_{val} is the valence angle energy; E_{tors} is torsion angle energy; E_{lp} is long-pair energy; $E_{\text{H-bond}}$ is hydrogen-bond energy. These terms are bond-order dependent. E_{vdW} and E_{Coulomb} are van der Waals energy and coulombic energy, which are bond-order independent.

The basic assumption of the ReaxFF method is that the bond order between a pair of atoms, BO_{ij}, can be directly obtained from the interatomic distance r_{ij}:

$$\text{BO}_{\text{ij}} = \text{BO}_{\text{ij}}^{\sigma} + \text{BO}_{\text{ij}}^{\pi} + \text{BO}_{\text{ij}}^{\pi\pi} = \exp\left[p_{\text{bo1}}\left(\frac{r_{\text{ij}}}{r_{\text{o}}^{\sigma}}\right)^{p_{\text{bo2}}}\right] + \exp\left[p_{\text{bo3}}\left(\frac{r_{\text{ij}}}{r_{\text{o}}^{\pi}}\right)^{p_{\text{bo4}}}\right] + \exp\left[p_{\text{bo5}}\left(\frac{r_{\text{ij}}}{r_{\text{o}}^{\pi\pi}}\right)^{p_{\text{bo6}}}\right] \quad (2)$$

where the three terms in the above equation correspond to the bond orders of the σ bond, the first π bond and the second π bond (π π); *i* and *j* refer to atom *i* and *j*; r_{o} is the equilibrium bond length; p_{bo} is the empirical parameter. Calculating bond orders in this way allows us to distinguish various contributions from σ bond, π bond and π π bond.

Short-range Pauli repulsion and long-range dispersion – the nonbonded interactions – are included in E_{vdW}. E_{Coulomb} is taken into account for all atom pairs. Charge values are determined at each time step, which makes it possible to describe charge transfer during a chemical reaction.

3.2 Computational details

Since the main component of ceramic is SiC, only SiC was considered in the reactive MD simulation. The simulation box contains a slab of SiC in the presence of solar salt. The SiC slab consists of 12 layers and each layer has 32 atoms. The vacuum region with 19.5 Å is filled with $NaNO_3$ and KNO_3 molecules. Previous studies have confirmed that the size effect of SiC can be ignored when the slab is larger than 11 layers with a 12.5 Å vacuum region [41]. One end of the SiC slab is Si-terminated while the other is C-terminated. $NaNO_3$/KNO_3 is placed at the end sides of the SiC slab. This configuration enables the possible chemical reaction of both Si and

C species. The salt system at each end consists of 45 $NaNO_3$ molecules and 25 KNO_3 molecules. The mass ratio is about 6: 4, which is consistent with the real solar salt.

The Large-scale Atomic/Molecular Massively Parallel Simulator (LAMMPs) package was used to conduct all the simulations [42]. Simulations were carried out in NVT ensemble with a timestep of 0.25 fs and Nosè-Hoover thermostat. Periodic boundary conditions were employed in three dimensions and the conjugate gradient algorithm was used for energy minimization. The ReaxFF force field developed by Newsome et al. [39] was adopted in this study. The system was first heated to 300℃ and maintained for 1ns; then it was cooled to 150℃. Finally, the system was kept at 150℃ for 1ns. The heating/cooling was carried out 50, 100, 150 and up to 200 times to reproduce the charging/discharging procedure. The damping parameter which determines how rapidly the temperature was relaxed was set as 100 fs.

4. Results and discussions

4.1 Heat transfer performance

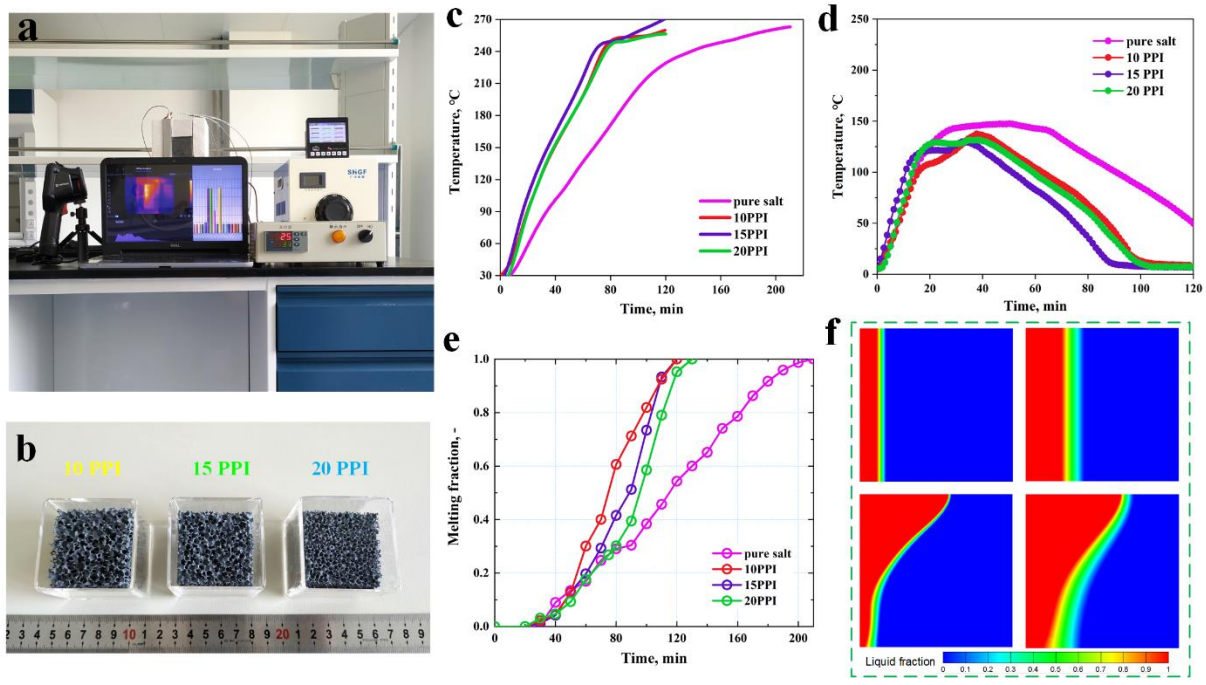

Figure 2. (a) The setup of phase change heat transfer experiments. (b) Porous ceramic skeleton with the pore size of 10 PPI, 15 PPI and 20 PPI. (c) Variation of the temperature at point P2. (d) Temperature difference between points P1 and P3. (e) Variation of melting fraction with time. (f) Comparison of the contribution of

heat conduction and natural convection to the phase change at t = 3600s. The left two figures are the simulated solid-liquid phase fields of pure solar salt and the right figures are results of the 10 PPI composite. The top two figures only consider heat conduction while the bottom figures consider both heat conduction and natural convection.

Figure 2(c) shows the variation of the temperature at point P2. It is seen that the temperature increases rapidly at the early stage; when the PCM starts to melt, the temperature rise gets slow. And the temperature of composites is obviously higher than that of pure salt because in composite PCMs, the heat can be quickly transferred from the heating wall to the interior. The temperature difference between points P1 and P3 is presented in Figure 2(d). The temperature difference reflects the uniformity of the temperature distribution. The maximum temperature difference in pure solar salt can reach up to 148℃, while in composites, it can be reduced to 130℃. Moreover, in most stages of melting, the temperature difference of composites is obviously lower than that of pure salt. The temperature difference curves of composites PCMs do not follow the order 10 PPI > 15 PPI > 20 PPI or 10 PPI < 15 PPI < 20 PPI. It may be attributed to the contrary effects of the pore size. On the one hand, the large pore benefits the fluid flow and enhances the natural convection; on the other hand, the large pore means less contact area of the skeleton with PCM, which harms transferring heat from the skeleton to PCM. These two roles are contrary. Therefore, the variation of temperature difference curves is not consistent with the trend of the pore sizes.

Figure 2(e) shows the melting fraction of composites and pure salt. The melting fraction was determined based on the area occupied by the solid and liquid PCMs in the digital images [43]. The ImageJ software was used to process the images to identify the pixel-areas of solid and liquid PCMs. It is seen from Figure 2(e) that the complete melting time of the pure salt is 210 min. 10 PPI and 15 PPI composites have the shortest melting time, 120 min, and the melting rate is increased by 42.9%.

To make clear the contribution of heat conduction and natural convection to the phase change heat transfer, a representative elementary volume (REV)-scale simulation was performed. The detailed computational methodology can be found in Supporting Information. The simulated solid-liquid phase interface at t = 3600s is presented in Figure 2(f). When only heat conduction is considered, the solid-liquid interface is always parallel to the heating wall, as the top two figures show. When both heat conduction and natural convection are considered, the solid-liquid interface is obviously curved and the melting rate of PCM in the upper portion is faster than that in the lower portion. This is because the hot liquid PCM is driven by the buoyancy force and flows upwards along the heating wall; it accumulates in the upper portion and accelerates the melting [2].

For the only heat conduction case, the liquid fraction of the pure salt is 0.14 while that of the ceramic/salt composite is 0.30. It suggests that the ceramic skeleton enhances heat conduction significantly. When natural convection is considered, the liquid fraction of the pure salt is 0.26 while that of the ceramic/salt composite is 0.41. In terms of the pure salt, the contribution of heat conduction to melting is 53.8%; by contrast, for the ceramic/salt composite, the value is 73.2%. The contribution of heat conduction is obviously increased. And due to the large pore configuration, the solid-liquid interface of the ceramic/salt composite is still curved, suggesting that the natural convection is not restricted seriously. As a result, the overall heat transfer is enhanced.

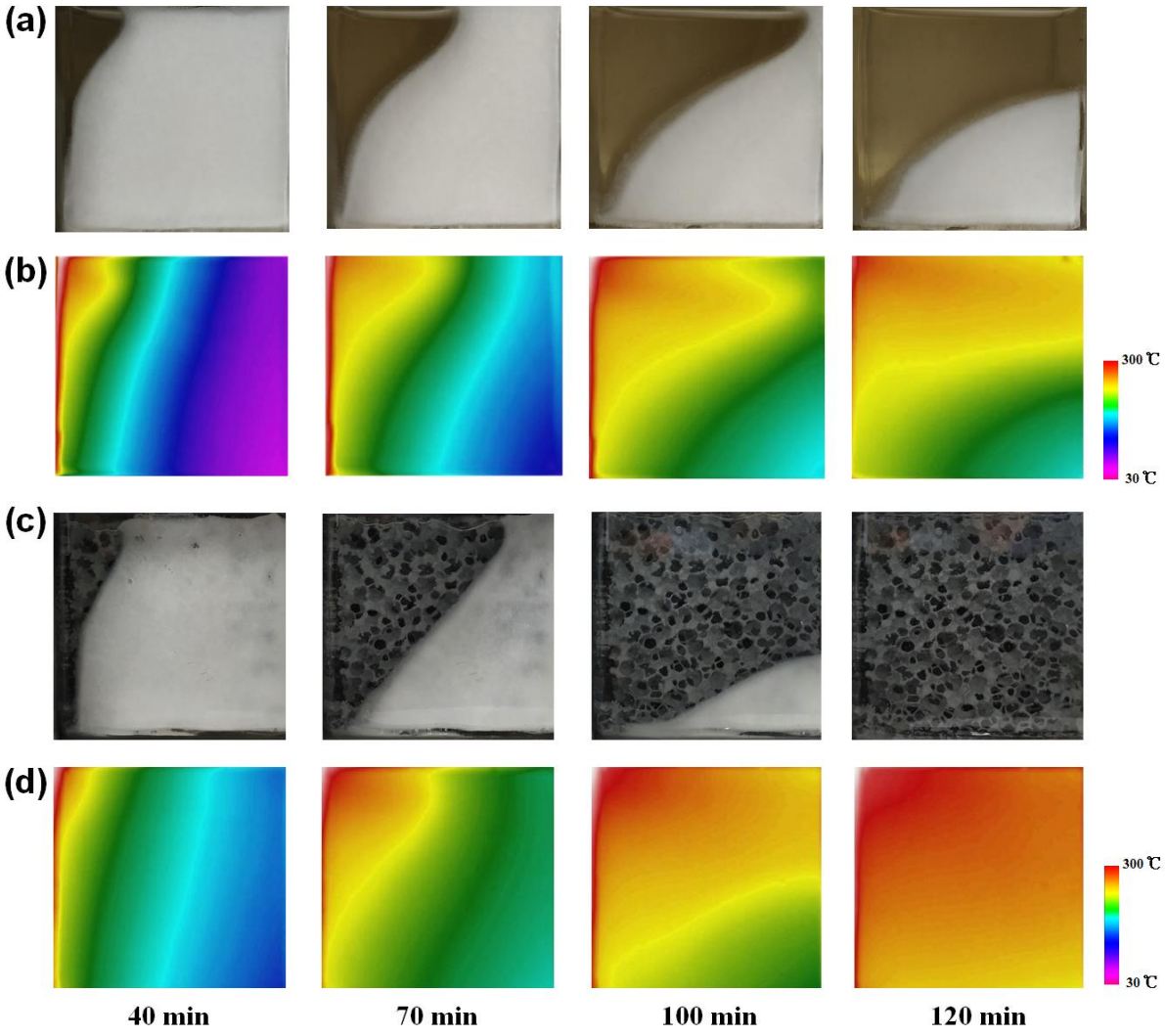

Figure 3. Evolution of solid-liquid phase interface and temperature field. (a)-(b): Phase interface of pure solar salt and temperature field captured by the infrared camera; (c)-(d): phase interface of solar salt/15 PPI porous ceramic composite and temperature field.

The evolution of the solid-liquid phase interface is presented in **Figure 3**(a) and (c). The temperature field of the front surface of the cavity was captured by the infrared camera and the results are shown in Figures 3(b) and (d). It is seen from Figure 3(a)-(b) that the solid-liquid interface is curved and the temperature of the top region is higher. This is due to the natural convection: the hot liquid salt flows upwards driven by the buoyancy force and downwards along the solid-liquid interface, forming a circulatory region; thermal energy in hot liquid PCM is released during the downwards flow process and more energy is absorbed by the upper part

of the interface; as a result, the melting rate of the upper region is higher and the solid-liquid interface is sloped [44].

After embedding the ceramic matrix into salt, the heat transfer enhancement is obvious. The melting fraction of composites is larger than that of pure salt, for example, at t = 110 min, the melting fraction of 15 PPI composite PCM is 0.925 while that of pure salt is only 0.457. Moreover, the heat can be efficiently transferred to the inside. The temperature field is more uniform and the temperature difference is decreased. This is very important because it can avoid local overheating and mitigate thermal stress fatigue failure, which will extend the life cycle of the equipment.

4.2 Corrosion analysis

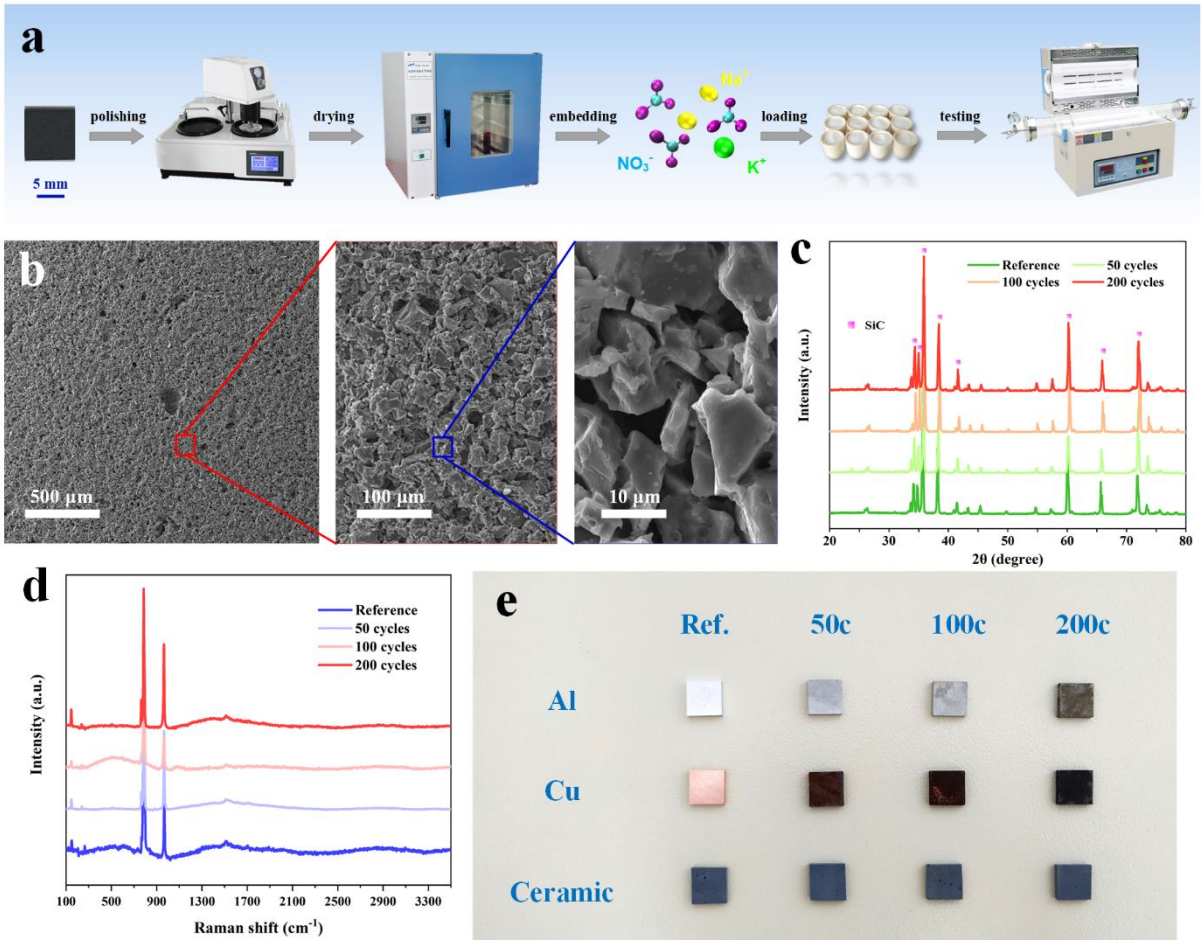

Figure 4. (a) Schematic of the corrosion test process. (b) Surface morphology of the ceramic in the reference group. (c) XRD patterns of the ceramics under various test conditions. (d) Raman spectroscopy of different ceramic samples. (e) Photographs of ceramic, Al and Cu pieces under different heating/cooling cycles.

Figure 4(a) presents the flow chart of the corrosion test. The ceramic pieces were characterised using SEM, EDS, XRD and Raman to investigate the corrosion behaviours. The surface morphology of the ceramic in the reference group is shown in Figure 4(b). It is seen that there are many pores distributing on the surface of the ceramic. The size of the largest pore exceeds 100 μm while the size of the smallest pores is less than 1 μm. Although the ceramic piece has been polished, the surface is still uneven. According to Wenzel's wetting theory [45], the surface roughness enhances wettability. The rough surface of the ceramic may be one of the reasons for the excellent wettability. Moreover, this highly porous configuration increases the contact area with PCM and benefits enhancing heat transfer.

The surface morphologies of ceramics under various heating/cooling cycles are presented in **Figure 5**. It is seen that ceramics in the corrosion test groups have many pores on the surface, which is similar to the reference group. From the high magnification image, the edges of SiC grains are sharp. The angular structure of SiC grains can be observed in both the reference group and the test groups, suggesting that SiC grains are not corroded by molten salt. It is seen from EDS mappings that Si and O elements distributes uniformly on the ceramic surface; other elements including C, Na, K and N also distribute uniformly, as Figures S4-S6 show. These elements do not aggregate significantly, indicating that there are no or little corrosion products on the surface.

The XRD patterns of ceramics are presented in Figure 4(c). The peak at 2θ = 34.09°, 34.72°, 35.65°, 38.13°, 41.38°, 59.99°, 65.62° and 71.74° corresponds to the surface (3 1 1), (1 0 1), (0 0 4), (1 0 2), (4 0 0), (1 1 0), (1 0 6) and (1 1 4) of SiC respectively [46]. The diffraction peaks are narrow and sharp, indicating high crystallinity. After the corrosion test, no new phase forms

and the main phases are still SiC. And the diffraction peaks remain sharp, indicating there are no defects caused by corrosion and the structure of SiC crystal is stable.

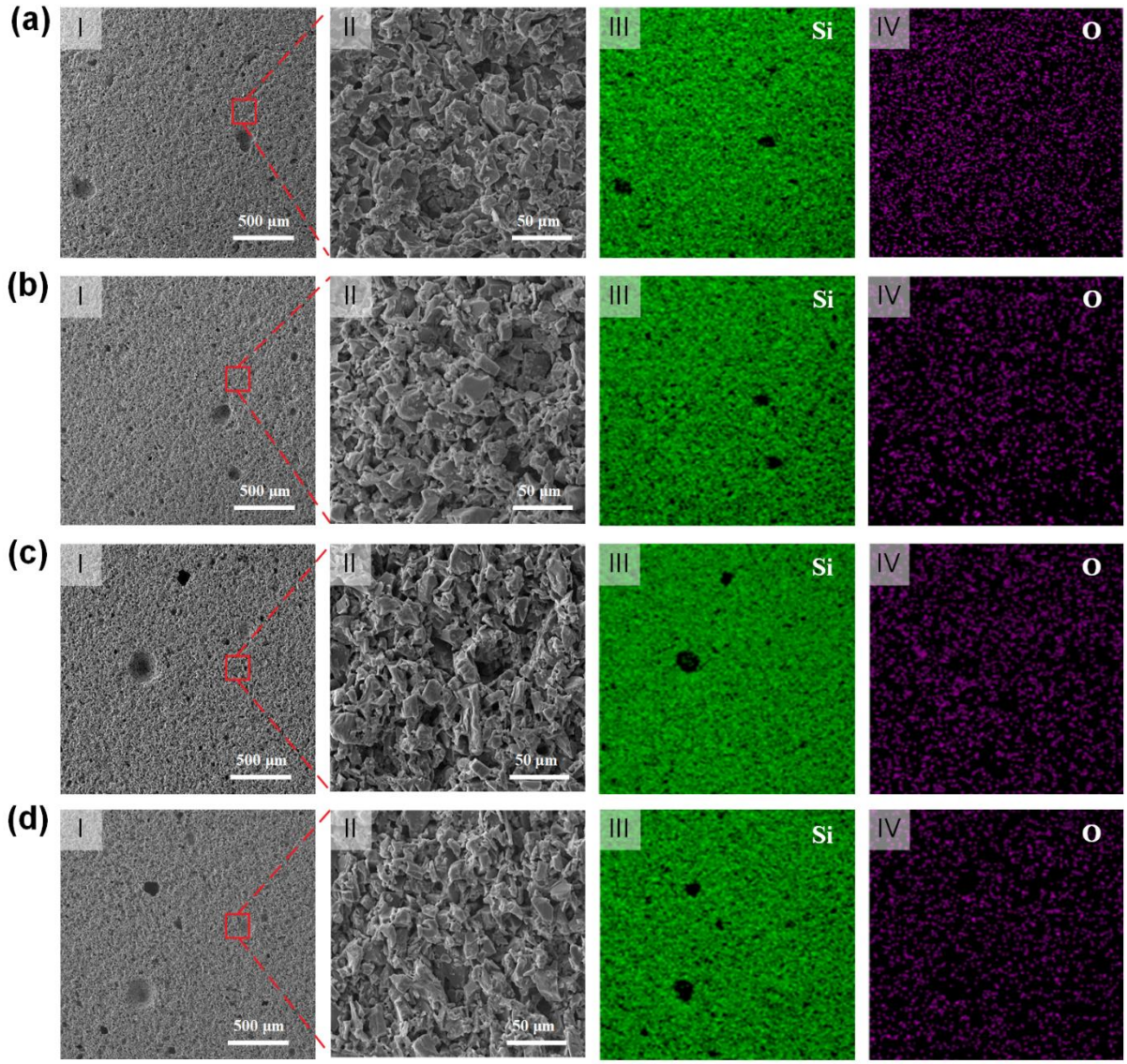

Figure 5. Surface morphology and EDS mappings of ceramic pieces: (a) the reference group, (b) 50 heating/cooling cycles group, (c) 100 cycles group and (d) 200 cycles group.

Figure 4(d) shows the Raman spectroscopy of ceramic samples. For the reference group, the Raman scattering mainly occurs at shifts = 786 cm^{-1} and 964 cm^{-1}, which corresponds to the transverse optical and longitudinal optical of SiC [47]. Some weak Raman bands are found at 147 cm^{-1} and 766 cm^{-1}, which may be associated with disorder crystals and impurities [48].

After the corrosion test, the Raman features of ceramics are almost unchanged, indicating the low degree of reaction between the ceramic and solar salt.

Cu and Al – the widely used thermal promoters in low-temperature PCMs – are also tested and the results are shown in Figure 4(e). After 50 cycles, the surface of Al and Cu pieces becomes dull. As the cycle number increases, the metal is corroded more seriously. In contrast, the surface of the ceramic remains almost unchanged. It can be concluded from the above results that the ceramic exhibits excellent anti-corrosion performance.

4.3 Molecular simulations

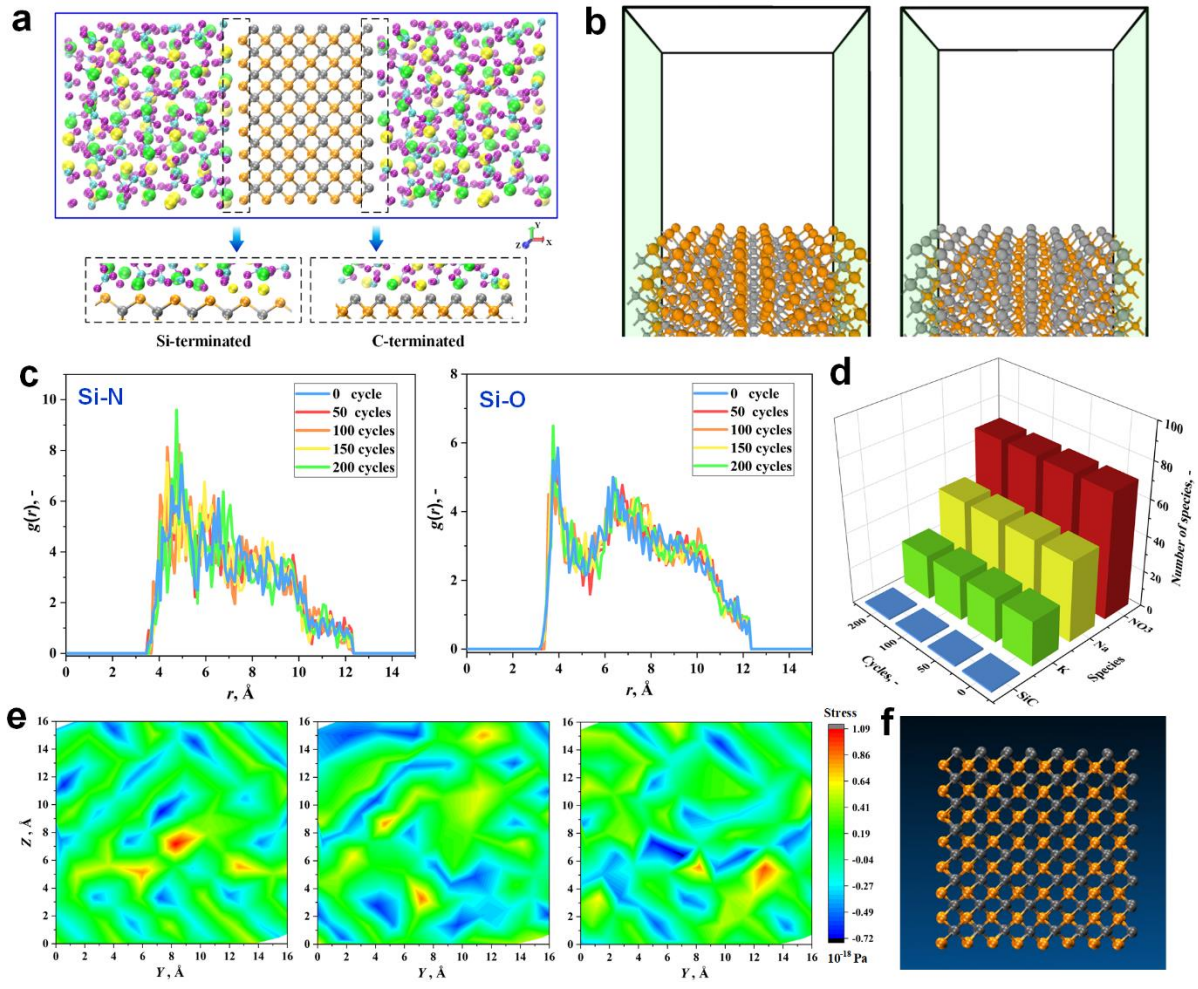

Figure 6. (a) A snapshot of the simulation box. Gray, orange, yellow, green, purple and cyan spheres represent C, Si, Na, K, O and N atoms respectively. (b) Morphology of SiC after 200 heating/cooling cycles. From left to right is the Si-terminated and C-terminated domain respectively. (c) Radial distribution functions of Si-N and Si-O pairs in the Si-terminated domain. (d) The number of various species during the simulation.

(e) Shearing stress distribution of SiC surface during the cooling process. The left to right figure represents the condition at 300℃, 220℃ and 150℃ respectively. (f) A snapshot of SiC along the [1 0 0] direction after 200 cycles. The colour code is the same as that in Figure 6(a).

Figure 6(a) illustrates a snapshot of the simulation box. Figure 6(b) shows the morphology of SiC after 200 heating/cooling cycles from the MD simulation results. It is seen that Si and C species do not physically dissolve into the salt. It may be attributed to the fact that SiC is a covalent network compound [49] and the bonding energy is very high, up to 135 kcal/mol [50]. The strong covalent bond makes it difficult for Si and C atoms to separate from the bulk. Radial distribution functions (RDFs) of SiC and salt species pairs are calculated. Figure 6(c) shows the RDFs of Si-N and Si-O pairs in the Si-terminated domain. Since the surface atoms of SiC are more likely to react, only the surface Si atoms in the Si-terminated domains are counted in the calculation of radial distribution functions. And the salt domain is divided into five layers according to the distance from the SiC surface. Salt species in the nearest layer are counted. It is seen from Figure 6(c) that the minimum distance of Si-N pairs at the initial state is 3.55 Å. After 50, 100, 150 and 200 cycles, the distance of Si-N pairs does not get shortened. For the possible products, i.e. Si_3N_4, the length of the Si-N bond is 1.75 Å [51]. It indicates that the Si and N species are not bonded. The minimum distance of Si-O pairs is 3.25 Å. The bond length of Si-O in SiO_2, the possible product, is 1.61 Å [52], suggesting that the Si and O species are also not bonded. In the C-terminated domain, the minimum distance of C-N and C-O pairs does not change after heating/cooling cycles, as Figure S7 shows. All the RDF results indicate that there are no new bonds formed between SiC and solar salt.

The possible chemical reaction was monitored by detecting the number of chemical species during the ReaxFF molecular dynamics [53]. It is seen from Figure 6(d) that the number of SiC is constant 1. This is because SiC is a covalent network compound [49]: one Si atom bonds with the neighbouring four C atoms each of which also bonds with the neighbouring four

Si atoms, resulting in a covalent network. So, they are identified as one molecule (Si192C192). During the simulation, the number of various species does not change, indicating no chemical reaction occurring between SiC and $NaNO_3$/KNO_3.

The thermal stress induced by heating/cooling cycles would accelerate the corrosion [54]. Therefore, the effect of thermal stress on corrosion behaviours is investigated. Figure 6(e) shows the shear stress (τ_{xy}) field of the SiC surface during the cooling process. It is seen that the stress field does not change significantly when the temperature decreases from 300℃ to 220℃ and ultimately to 150℃. It may be attributed to the excellent thermal conduction of SiC [55]. Heat can be efficiently transferred from the surface to the inner material and the temperature difference between the surface and core is small, which will not generate a large stress gradient. Moreover, the coefficient of thermal expansion of SiC is only 3.69×10^{-6} /℃ (150 ℃) [56], which further weakens the influence of thermal stress. A snapshot of SiC after 200 cycles is presented in Figure 6(f). Although some atoms slightly deviate from the initial lattice point, there are no dislocations and defects forming in SiC, which indicates the stable structure of SiC.

5. Conclusions

Molten salts have been widely used as energy storage materials in medium- and high-temperature thermal energy storage systems. However, due to their high corrosivity and the extremely high-temperature environment, current methods for enhancing heat transfer do not apply. In the current study, SiC ceramic was used as the thermal promoter and integrated with solar salt to fabricate composite phase change materials. The porous ceramic skeleton has the characteristics of open cells, high porosity and large pore configuration. The prepared ceramics exhibit excellent wettability to solar salt, so that the impregnation of salt into ceramic achieves a high loading at atmospheric pressure. The phase change heat transfer characteristics were revealed, including temperature evolution, melting fraction, solid-liquid phase interface and

temperature field. Compared to pure solar salt, the overall phase change rate of composite PCMs is increased by 42.9%. Corrosion behaviours of ceramics were studied by conducting up to 200 heating/cooling cycles. Cu and Al – the widely used thermal promoters for low-temperature PCMs – were also tested. Results of SEM, EDS, XRD and Raman indicate that ceramics have excellent corrosion-resistant performance. Finally, a reactive molecular dynamics simulation was performed to provide microscopic insights into corrosion behaviours of SiC ceramic including the possible physical dissolution, chemical reaction and thermal stress failure. Ceramic/ solar salt composite PCMs possess advantages of simple preparation, low cost and easy maintenance, therefore have great potential for large-scale applications.

Acknowledgements

The authors would like to acknowledge the financial support by National Key R&D Program of China (No. 2018YFA0702300), H2020-MSCA-RISE-778104–ThermaSMART, Ningbo Science and Technology Bureau (No. 2019B10042), doctoral degree scholarship of China Scholarship Council (CSC). We are grateful for access to the University of Nottingham's Augusta HPC service.

Conflicts of interest

There are no conflicts to declare.

Nomenclature

BO	Bond order
CMC	Carboxymethylcellulose sodium
EDS	Energy-dispersive spectroscopy
LAMMPS	Large-scale Atomic/Molecular Massively Parallel Simulator
MD	Molecular dynamics
PCM	Phase change material
PPI	Pores per inch
PU	Polyurethane
QM	Quantum mechanics
RDF	Radial distribution function
REV	Representative elementary volume
SEM	Scanning electron microscope
SiC	Silicon carbide
ss-PCM	Shape-stabilised phase change material
TES	Thermal energy storage
XRD	X-ray diffraction
E_{bond}	Bond energy
E_{under}	Undercoordination penalty energy
E_{over}	Overcoordination penalty energy
E_{val}	Valence angle energy
E_{tors}	Torsion angle energy
E_{lp}	Long-pair energy

$E_{\text{H-bond}}$	Hydrogen-bond energy
E_{vdW}	Van der Waals energy
E_{Coulomb}	Coulombic energy
p_{bo}	Empirical parameter
r_{o}	Equilibrium bond length

Subscripts

i, j	Atom i and j
σ	σ bond
π	The first π bond
ππ	The second π bond

References

[1] H. Zhang, J. Baeyens, G. Cáceres, J. Degreve, Y. Lv, Thermal energy storage: Recent developments and practical aspects, Prog Energy Combust Sci, 53 (2016) 1-40.

[2] S. Zhang, D. Feng, L. Shi, L. Wang, Y. Jin, L. Tian, Z. Li, G. Wang, L. Zhao, Y. Yan, A review of phase change heat transfer in shape-stabilized phase change materials (ss-PCMs) based on porous supports for thermal energy storage, Renew Sust Energ Rev, 135 (2021) 110127.

[3] P. Zhang, X. Xiao, Z.W. Ma, A review of the composite phase change materials: Fabrication, characterization, mathematical modeling and application to performance enhancement, Appl Energ, 165 (2016) 472-510.

[4] S. Zhang, Y. Jin, Y. Yan, Depression of melting point and latent heat of molten salts as inorganic phase change material: Size effect and mechanism, J Mol Liq, 20 (2021) 117058.

[5] S. Zhang, Y. Yan, Melting and thermodynamic properties of nanoscale binary chloride salt as high-temperature energy storage material, Case Stud Therm Eng, 25 (2021) 100973.

[6] J. Ding, G. Pan, L. Du, J. Lu, X. Wei, J. Li, W. Wang, J. Yan, Theoretical prediction of the local structures and transport properties of binary alkali chloride salts for concentrating solar power, Nano Energy, 39 (2017) 380-389.

[7] S. Guillot, A. Faik, A. Rakhmatullin, J. Lambert, E. Veron, P. Echegut, C. Bessada, N. Calvet, X. Py, Corrosion effects between molten salts and thermal storage material for concentrated solar power plants, Appl Energ, 94 (2012) 174-181.

[8] L. Miró, J. Gasia, L.F. Cabeza, Thermal energy storage (TES) for industrial waste heat (IWH) recovery: A review, Appl Energ, 179 (2016) 284-301.

[9] C. Li, Q. Li, Y. Li, X. She, H. Cao, P. Zhang, L. Wang, Y. Ding, Heat transfer of composite phase change material modules containing a eutectic carbonate salt for medium and high temperature thermal energy storage applications, Appl Energ, 238 (2019) 1074-1083.

[10] G. Alva, L. Liu, X. Huang, G. Fang, Thermal energy storage materials and systems for solar energy applications, Renew Sust Energ Rev, 68 (2017) 693-706.

[11] J.M. Mahdi, S. Lohrasbi, E.C. Nsofor, Hybrid heat transfer enhancement for latent-heat thermal energy storage systems: A review, Int J Heat Mass Tran, 137 (2019) 630-649.

[12] V. Joshi, M.K. Rathod, Experimental and numerical assessments of thermal transport in fins and metal foam infused latent heat thermal energy storage systems: A comparative evaluation, Appl Therm Eng, 178 (2020) 115518.

[13] Y. Yao, H. Wu, Interfacial heat transfer in metal foam porous media (MFPM) under steady thermal conduction condition and extension of Lemlich foam conductivity theory, Int J Heat Mass Tran, 169 (2021) 120974.

[14] Y. Yao, H. Wu, Z. Liu, Direct Simulation of Interstitial Heat Transfer Coefficient Between Paraffin and High Porosity Open-Cell Metal Foam, J Heat Transfer, 140(3) (2018) 032601.

[15] Y. Yao, H. Wu, Thermal transport process of metal foam/paraffin composite (MFPC) with solid-liquid phase change: An experimental study, Appl Therm Eng, 179 (2020) 115668.

[16] R. Fukahori, T. Nomura, C. Zhu, N. Sheng, N. Okinaka, T. Akiyama, Thermal analysis of Al–Si alloys as high-temperature phase-change material and their corrosion properties with ceramic materials, Appl Energ, 163 (2016) 1-8.

[17] Y. Zhao, H.B. Liu, C.Y. Zhao, Experimental study on the cycling stability and corrosive property of Al-Si alloys as phase change materials in high-temperature heat storage, Sol Energ Mat Sol C, 203 (2019) 110165.

[18] H. Xu, F. Dal Magro, N. Sadiki, J.-M. Mancaux, X. Py, A. Romagnoli, Compatibility study between aluminium alloys and alternative recycled ceramics for thermal energy storage applications, Appl Energ, 220 (2018) 94-105.

[19] I. Ortega-Fernández, Y. Grosu, A. Ocio, P.L. Arias, J. Rodríguez-Aseguinolaza, A. Faik, New insights into the corrosion mechanism between molten nitrate salts and ceramic materials

for packed bed thermocline systems: A case study for steel slag and Solar salt, Sol Energy, 173 (2018) 152-159.

[20] S. Liu, H. Yang, Porous ceramic stabilized phase change materials for thermal energy storage, RSC Adv, 6(53) (2016) 48033-48042.

[21] Y. Jiang, Y. Sun, R.D. Jacob, F. Bruno, S. Li, Novel Na2SO4-NaCl-ceramic composites as high temperature phase change materials for solar thermal power plants (Part I), Sol Energ Mat Sol C, 178 (2018) 74-83.

[22] H. Wang, X. Ran, Y. Zhong, L. Lu, J. Lin, G. He, L. Wang, Z. Dai, Ternary chloride salt–porous ceramic composite as a high-temperature phase change material, Energy, 238 (2022) 121838.

[23] G. Xu, G. Leng, C. Yang, Y. Qin, Y. Wu, H. Chen, L. Cong, Y. Ding, Sodium nitrate – Diatomite composite materials for thermal energy storage, Sol Energy, 146 (2017) 494-502.

[24] F. Jiang, Z. Ge, X. Ling, D. Cang, L. Zhang, Y. Ding, Improved thermophysical properties of shape-stabilized NaNO3 using a modified diatomite-based porous ceramic for solar thermal energy storage, Renew Energ, 179 (2021) 327-338.

[25] X. Yang, Q. Bai, Z. Guo, Z. Niu, C. Yang, L. Jin, T.J. Lu, J. Yan, Comparison of direct numerical simulation with volume-averaged method on composite phase change materials for thermal energy storage, Appl Energ, 229 (2018) 700-714.

[26] H. Zheng, C. Wang, Q. Liu, Z. Tian, X. Fan, Thermal performance of copper foam/paraffin composite phase change material, Energ Convers Manage, 157 (2018) 372-381.

[27] P. Zhang, Z.N. Meng, H. Zhu, Y.L. Wang, S.P. Peng, Melting heat transfer characteristics of a composite phase change material fabricated by paraffin and metal foam, Appl Energ, 185 (2017) 1971-1983.

[28] S. Zhang, Z. Li, H. Wang, L. Tian, Y. Jin, M. Alston, Y. Yan, Component-dependent thermal properties of molten salt eutectics for solar thermal energy storage: experiments, molecular simulation and applications, Appl Therm Eng, (2022) 118333.

[29] Y. Xu, Q. Ren, Z.-J. Zheng, Y.-L. He, Evaluation and optimization of melting performance for a latent heat thermal energy storage unit partially filled with porous media, Appl Energ, 193 (2017) 84-95.

[30] R. Cozzolino, D. Chiappini, G. Bella, Experimental characterisation of a novel thermal energy storage based on open-cell copper foams immersed in organic phase change material, Energ Convers Manage, 200 (2019) 112101.

[31] Y. Yao, H. Wu, Z. Liu, Z. Gao, Pore-scale visualization and measurement of paraffin melting in high porosity open-cell copper foam, Int J Therm Sci, 123 (2018) 73-85.

[32] C.Y. Zhao, Z.G. Wu, Heat transfer enhancement of high temperature thermal energy storage using metal foams and expanded graphite, Sol Energ Mat Sol C, 95(2) (2011) 636-643.

[33] F. Ren, Z. Wang, Z. Ma, J. Su, F. Li, L. Wang, Effects of Fe2O3 concentration on microstructures and properties of SiC-based ceramic foams, Mater Sci Eng, A, 515(1) (2009) 113-116.

[34] T.P. Senftle, S. Hong, M.M. Islam, S.B. Kylasa, Y. Zheng, Y.K. Shin, C. Junkermeier, R. Engel-Herbert, M.J. Janik, H.M. Aktulga, T. Verstraelen, A. Grama, A.C.T. van Duin, The ReaxFF reactive force-field: development, applications and future directions, npj Comput Mater, 2(1) (2016) 15011.

[35] K. Chenoweth, A.C.T. van Duin, W.A. Goddard, ReaxFF Reactive Force Field for Molecular Dynamics Simulations of Hydrocarbon Oxidation, J Phys Chem A, 112(5) (2008) 1040-1053.

[36] K.D. Nielson, A.C.T. Van Duin, J. Oxgaard, W.-Q. Deng, W.A. Goddard, Development of the ReaxFF reactive force field for describing transition metal catalyzed reactions, with

application to the initial stages of the catalytic formation of carbon nanotubes, J Phys Chem A, 109(3) (2005) 493-499.

[37] D. Kumar, V. Jain, B. Rai, Capturing the synergistic effects between corrosion inhibitor molecules using density functional theory and ReaxFF simulations - A case for benzyl azide and butyn-1-ol on Cu surface, Corros Sci, 195 (2022) 109960.

[38] S. Bhoi, T. Banerjee, K. Mohanty, Molecular dynamic simulation of spontaneous combustion and pyrolysis of brown coal using ReaxFF, Fuel, 136 (2014) 326-333.

[39] D.A. Newsome, D. Sengupta, H. Foroutan, M.F. Russo, A.C.T. van Duin, Oxidation of Silicon Carbide by O2 and H2O: A ReaxFF Reactive Molecular Dynamics Study, Part I, J Phys Chem C, 116(30) (2012) 16111-16121.

[40] O. Assowe, O. Politano, V. Vignal, P. Arnoux, B. Diawara, O. Verners, A.C.T. van Duin, Reactive Molecular Dynamics of the Initial Oxidation Stages of Ni(111) in Pure Water: Effect of an Applied Electric Field, J Phys Chem A, 116(48) (2012) 11796-11805.

[41] J. Xi, H. Jiang, C. Liu, D. Morgan, I. Szlufarska, Corrosion of Si, C, and SiC in molten salt, Corros Sci, 146 (2019) 1-9.

[42] D. Hu, T. Gu, Z. Cui, S. Vollebregt, X. Fan, G. Zhang, J. Fan, Insights into the high-sulphur aging of sintered silver nanoparticles: An experimental and ReaxFF study, Corros Sci, 192 (2021) 109846.

[43] M. Al-Jethelah, S. Ebadi, K. Venkateshwar, S.H. Tasnim, S. Mahmud, A. Dutta, Charging nanoparticle enhanced bio-based PCM in open cell metallic foams: An experimental investigation, Appl Therm Eng, 148 (2019) 1029-1042.

[44] Y. Yao, H. Wu, Macroscale Modeling of Solid–Liquid Phase Change in Metal Foam/Paraffin Composite: Effects of Paraffin Density Treatment, Thermal Dispersion, and Interstitial Heat Transfer, J Therm Sci Eng Appl, 13(4) (2021).

[45] R.N. Wenzel, Resistance of solid surfaces to wetting by water, Ind Eng Chem, 28(8) (1936) 988-994.

[46] U. Soy, A. Demir, F. Caliskan, Effect of Bentonite Addition on Fabrication of Reticulated Porous SiC Ceramics for Liquid Metal Infiltration, Ceram Int, 37 (2011) 15-19.

[47] S. Nakashima, H. Harima, Raman Investigation of SiC Polytypes, Phys Status Solidi A, 162(1) (1997) 39-64.

[48] Y. Qin, X. Li, C. Liu, C. Zheng, Q. Mao, B. Chen, K. Jing, Y. Tan, L. Cheng, L. Zhang, Effect of deposition temperature on the corrosion behavior of CVD SiC coatings on SiCf/SiC composites under simulated PWR conditions, Corros Sci, 181 (2021) 109233.

[49] V.A. Izhevskyi, L.A. Genova, J.C. Bressiani, A.H.A. Bressiani, silicon carbide. Structure, properties and processing, Cerâmica, 46(297) (2000) 4-13.

[50] H. Tanaka, Y. Uemura, Y. Inomata, Observations of holes around dislocation core in SiC crystal, J Cryst Growth, 53(3) (1981) 630-632.

[51] Q. Fan, C. Chai, Q. Wei, P. Zhou, Y. Yang, Elastic anisotropy and electronic properties of Si3N4 under pressures, AIP Adv, 6(8) (2016) 085207.

[52] H. Ohsaki, K. Miura, A. Imai, M. Tada, M.A. Aegerter, Structural analysis of SiO 2 gel films by high energy electron diffraction, J Sol-Gel Sci Technol, 2(1) (1994) 245-249.

[53] N. Farzi, M.-H. Hydarifard, M.E. Izadi, H. Sabzyan, Investigation of iron carbide (Fe3C) corrosion in water and acidic solution using ReaxFF molecular dynamics, J Mol Liq, 318 (2020) 114006.

[54] H.-z. Chen, B.-r. Li, B. Wen, Q. Ye, N.-q. Zhang, Corrosion resistance of iron-chromium-aluminium steel in eutectic molten salts under thermal cycling conditions, Corros Sci, 173 (2020) 108798.

[55] H. Nakano, K. Watari, Y. Kinemuchi, K. Ishizaki, K. Urabe, Microstructural characterization of high-thermal-conductivity SiC ceramics, J Eur Ceram Soc, 24(14) (2004) 3685-3690.

[56] Z. Li, R.C. Bradt, Thermal expansion of the cubic (3C) polytype of SiC, J Mater Sci, 21(12) (1986) 4366-4368.